Results in Physics 19 (2020) 103499

Contents lists available at ScienceDirect

Results in Physics

journal homepage: www.elsevier.com/locate/rinp

# Generation of low-order Laguerre-Gaussian beams using hybrid-machined reflective spiral phase plates for intense laser-plasma interactions

Ji Yong Bae [a], Cheonha Jeon [b], Ki Hong Pae [b,c], Chul Min Kim [b,c], Hong Seung Kim [a], Ilkyu Han [a], Woo-Jong Yeo [a], Byeongjoon Jeong [a], Minwoo Jeon [a], Dong-Ho Lee [a], Dong Uk Kim [a], Sangwon Hyun [a], Hwan Hur [a], Kye-Sung Lee [a], Geon Hee Kim [a], Ki Soo Chang [a], Il Woo Choi [b,c], Chang Hee Nam [b,d], I Jong Kim [a,*]

[a] Division of Scientific Instrumentation and Management, Korea Basic Science Institute, 169–148 Gwahak-ro, Yuseong-gu, Daejeon 34133, Republic of Korea
[b] Center for Relativistic Laser Science, Institute for Basic Science, 123 Cheomdangwagi-ro, Buk-gu, Gwangju 61005, Republic of Korea
[c] Advanced Photonics Research Institute, Gwangju Institute of Science and Technology, 123 Cheomdangwagi-ro, Buk-gu, Gwangju 61005, Republic of Korea
[d] Department of Physics and Photon Science, Gwangju Institute of Science and Technology, 123 Cheomdangwagi-ro, Buk-gu, Gwangju 61005, Republic of Korea

ARTICLE INFO

*Keywords:*
Laguerre-Gaussian vortex beam
Off-axis reflective spiral phase plate
Hybrid mechanical processing
Laser-plasma interaction
Orbital angular momentum
Spin angular momentum

ABSTRACT

In laser-plasma interactions (LPI), the laser beam mode is a critical parameter when trying to explore new physical phenomena. Of the various spatial beam modes, the Laguerre-Gaussian (LG) mode with vortex phase has attracted considerable attention due to its unique features, including the ability to carry an orbital angular momentum. Due to this, it has been actively applied to LPI, which mainly utilize ultrashort intense laser pulses. However, existing transmissive phase-manipulating optical elements have several limitations when applied in LPI due to critical issues such as pulse broadening, attenuation, and beam shape–all of which have an influence on the beam quality, as well as, geometry, size, simplicity, and cost–all of which are related to processing technologies. In this paper, we present a series of procedures to obtain high-quality low-order ($l = 1$ and 2) LG vortex beams from large-sized off-axis reflective spiral phase plates (ORSPPs). The geometric designs for various surface structures, electromagnetic wave simulations in the extra-large domain, hybrid-mechanical processing technique attempted newly, and experimental demonstrations are involved. Experimental observations of LG intensity distributions and interference fringes were verified with the simulation results of Poynting vector, phase, and angular momentum densities. The beam quality of LG intensity distributions was analyzed quantitatively through the investigation of an annular zone formed from the uniformity of the stepped and continuous surface structures of ORSPPs. Furthermore, we numerically investigated the physical phenomena on the high-intensity angular momentum transfer from light to matter, considering ORSPP–driven low-order LG vortex laser pulses, by performing 3D particle-in-cell simulations.

## Introduction

The spatial beam mode of an ultrashort and intense laser pulse is a crucial parameter when trying to characterize laser-plasma interactions (LPI) [1]. Of the various spatial beam modes, the Laguerre-Gaussian (LG) mode with vortex phase has attracted remarkable attention in the fields of optics and photonics, due to its unique features which can carry the orbital angular momentum (OAM) that is equivalent to $l\hbar$ per photon ($l$ is the topological charge number or quantum number, and $\hbar$ is the reduced Planck constant) and can form a doughnut-shaped intensity distribution that arises from converting the phase of the beam into a vortex shape. Consequently, these characteristics of the LG mode could provide a new way to control ultrashort intense LPI. Recently, LG vortex laser pulses have played a critical in number of fascinating research results, such as laser wakefield for efficient positron acceleration [2], intense high-harmonic vortices generation [3], efficient & low divergence ion acceleration [4,5], and plasma hologram [6], together with fundamental interests such as the angular momentum (AM) transfer from light to matter [7].

In research works related to optical vortices over the last 30 years, various phase-manipulating optical elements such as spiral phase plates (SPPs), q-plate, computer-generated holograms, metasurfaces,

* Corresponding author.
*E-mail address:* ijkim@kbsi.re.kr (I.J. Kim).

https://doi.org/10.1016/j.rinp.2020.103499
Received 24 July 2020; Received in revised form 16 September 2020; Accepted 11 October 2020
Available online 16 October 2020

plasmonic nanostructures, and spatial light modulators (SLMs) have been implemented to realize LG vortex beams [8]. Almost all of these elements have used nanostructures on their surfaces for effecting the phase manipulation, and they are mainly utilized in widespread applications on optics and photonics researches [9–12] that are based on relatively weak intensity laser beams. For LPI, however, mostly ultrashort high-intensity laser pulses could be applied to the surface of these optical elements. Thus, the nanostructures on the surfaces must be able to withstand laser damages without collapse in their structural integrity. To generate LG vortex laser pulses by applying ultrashort high-intensity laser pulses, Sueda et al. [13] developed, for the first time, a multilevel SPP manufactured using multi-stage vapor deposition processes that allowed the fabrication of relatively large-sized devices. This multilevel SPP, which is a transmissive optical element deposited by $SiO_2$, enables higher laser damage resistance against ultrashort high-intensity laser pulses. Unfortunately, apart from the issue about the securement of higher laser damage resistance via the fabrication of relatively large-sized devices, the ideal LG vortex laser pulse is not easily generated by merely applying transmissive optical elements that are predominantly fabricated via consecutive semiconductor processes [13,14]. This is because as the beam passes through a transmissive optical element, generally, the optical quality inside and outside the optical element can affect the transmitted beam shape, and beam attenuation due to absorption can occur. In addition, the pulse broadening caused by the material dispersion along with high-intensity driven nonlinear phenomena should be considered when applying ultrashort (e.g., femtosecond) high-intensity laser pulses [15]. Hence, the consideration of reflective optical elements that complement these weaknesses of transmissive optical elements is indispensable for the formation of LG vortex laser pulses in ultrashort intense LPI.

As a part of efforts to establish reflective optical elements, Campbell et al. [16] developed a spiral phase mirror for obtaining high-order LG vortex beams (mostly a few tens of $l$) at the normal incidence (on-axis) configuration. They manufactured the spiral phase mirror using the diamond turning based mechanical processes, bringing to the fore its advantages of structural design flexibility, high cost-effectiveness in large-size fabrication, and process simplicity, compared to ordinary semiconductor processes. Nonetheless, for ultrashort intense LPI, high-order LG vortex beams and an on-axis configuration are inappropriate when trying to acquire the highest intensity of LG vortex laser pulses and to organize the experimental setup, respectively. Therefore, the development of low-order LG vortex beams with an off-axis configuration is required. In 2019, we proposed and verified geometric designs for off-axis reflective SPPs (ORSPPs), used for generating low-order LG vortex beams, by performing numerical simulations [17]. However, from the point of view of fabrication, the realization of these designs for large-sized (over 100 mm diameter) ORSPPs is quite challenging regardless of the processing technique employed, unlike in the case of high-order vortex beams. The main reason for this is that the total spiral height of ORSPP ($h_r$) is proportional to $l$. In other words, in the case of the design having a stepped spiral structure with low-order $l$ (=1 or 2), each stepped spiral height of ORSPP ($h_{r\text{-}step}$) is within a few tens of nanometers, which makes its precise control very difficult during manufacturing. Particularly, SPPs designed to have a continuous spiral structure can be even more difficult to manufacture–regardless of being transmissive or reflective type. Because of this inscrutable difficulty, the fabrication of continuous SPPs has been thought to be unquestionably unfeasible, despite a theoretical possibility that can ideally acquire high-quality LG vortex beams [18]. It is because of this reason that most studies related to LG vortex beams using manufactured SPPs are confined to the utilization of stepped spiral structures [19]. Consequently, the ultra-precisely manufactured high-quality SPPs have to be preceded to obtain low-order uniformed LG vortex laser pulses with well-defined OAM, which are vital for ultrashort intense LPI.

Herein, we show a series of procedures, to obtain high-quality low-order LG vortex beams generated by large-sized ORSPPs, and to demonstrate numerically and experimentally their characteristics. As one of the most effective ways to actualize the aforementioned concepts of the ORSPPs, we adopt the hybrid-mechanical processing technique that is ultraprecision diamond turning machining-fast tool servo (DTM-FTS) processes and magnetorheological-fluid (MRF) polishing process. Characteristics of ORSPPs introduced in this study are proved by calculating the time-averaged Poynting vector, phase changes, and time-averaged AM densities, and by measuring the intensity and the interference fringes. As a preliminary study prior to full-scale experiment of LPI, we further analyze the physical phenomena occurred during AM transfer from light to matter for various low-order LG vortex laser pulse modes by conducting 3D particle-in-cell (PIC) simulations.

## Geometric design of ORSPPs

The equation that determines $h_r$ is different from the total spiral height of a transmissive SPP ($h_t$). For a transmissive SPP, the difference of the optical path length ($\Delta L$) between two normally incident beams becomes $\Delta L = (n_r - 1)h_t$, where $n_r$ is the real part of refractive index (see the top of Fig. 1A). Considering the phase difference $\Delta\phi_t = (2\pi/\lambda)\Delta L = (2\pi/\lambda)(n_r - 1)h_t$ in a transmissive SPP, $h_t$ becomes $h_t = \lambda/(n_r - 1)$ for $l = 1$ ($\Delta\phi = 2\pi$). In contrast, for ORSPP (here, the reflection angle equals to the incident angle regardless of material absorption [20,21]), the difference in the optical path length $\Delta L$ (sum of the blue line $x$ and red line $y$) between two obliquely incident beams becomes $\Delta L = 2h_r\cos\theta$, where $\theta$ is the incident angle (see the bottom of Fig. 1A) by applying the relation $\theta = \theta$" (reflected angle) and the trigonometrical functions regardless of absorption of SPP. Considering the phase difference $\Delta\phi_r = (2\pi/\lambda)\Delta L = (2\pi/\lambda)2h_r\cos\theta$ in ORSPP, $h_r$ for $l = 1$ ($\Delta\phi = 2\pi$) is given by:

$$h_r = \frac{\lambda}{2cos\theta} \tag{1}$$

For a He-Ne laser with a wavelength of $\lambda = 632.8$ nm, as $n_r = 1.46$ (fused silica at $\lambda = 632.8$ nm) and $\theta = 45°$, $h_t$ and $h_r$ for $l = 1$ are 1376 nm and 447 nm, respectively. Note that $h_r$ is as thin as 32% of $h_t$ at $\theta = 45°$ and the tendency $h_r/h_t = (n_r - 1)/(2\cos\theta) < 1$ continues up to $\theta = 76.5°$.

A laser beam with an arbitrary angle of incidence $\theta$ is obliquely incident on the surface of ORSPP, as shown at the top of Fig. 1B. In this case, the circular cross-section of the incident beam is changed to an elliptical cross-section (see yellow line) on the surface of ORSPP. As can be seen at the bottom of Fig. 1B, the inner circle with a violet solid line on the $x$-$y$ plane denotes the cross-section of the incident beam, whereas the ellipse with a yellow solid line (the minor radius of the ellipse in the $y$-axis is the same as the radius of the inner circle) indicates the beam cross-section on the surface of ORSPP. The large circle denoted by a dotted line represents the whole mechanical size of ORSPP. When the position ($x$, $y$) on the inner circle and the angle $\varphi$ with respect to the $x$-axis are defined, the position of projection on the ellipse is ($x$', $y$) and the angle with respect to the $x$-axis is $\varphi$'. Hence, the projection direction from the circle to the ellipse does not correspond to the point where the ellipse intersects with the extension line that connects (0, 0) with ($x$, $y$). The position ($x$', $y$) corresponds to the point where the ellipse intersects with the extension line parallel to the $x$-axis, which passes through the position ($x$, $y$).

The equation of the inner circle given by radius $\cos\theta$ is $x^2 + y^2 = \cos^2\theta$, and the equation of the ellipse given by major radius 1 and minor radius $\cos\theta$ is $x'^2 + \frac{y^2}{cos^2\theta} = 1$. If the coordinates are transformed from Cartesian to polar coordinate system, the position ($x$', $y$) is converted to ($r\cos\varphi$', $r\sin\varphi$'), and accordingly $x$, $y$, and $\varphi$' become $x = \pm\sqrt{cos^2\theta - y^2} = \pm\frac{cos^2\theta cos\varphi'}{\sqrt{cos^2\varphi' cos^2\theta + sin^2\varphi'}}$, $y = \pm rsin\varphi' = \pm\frac{sin\varphi' cos\theta}{\sqrt{cos^2\varphi' cos^2\theta + sin^2\varphi'}}$, and $\varphi' = \tan^{-1}[\tan\varphi/\sec\theta]$, respectively. As a result, the local height ($H$) at a certain angle ($\varphi$') in ellipse is given by:

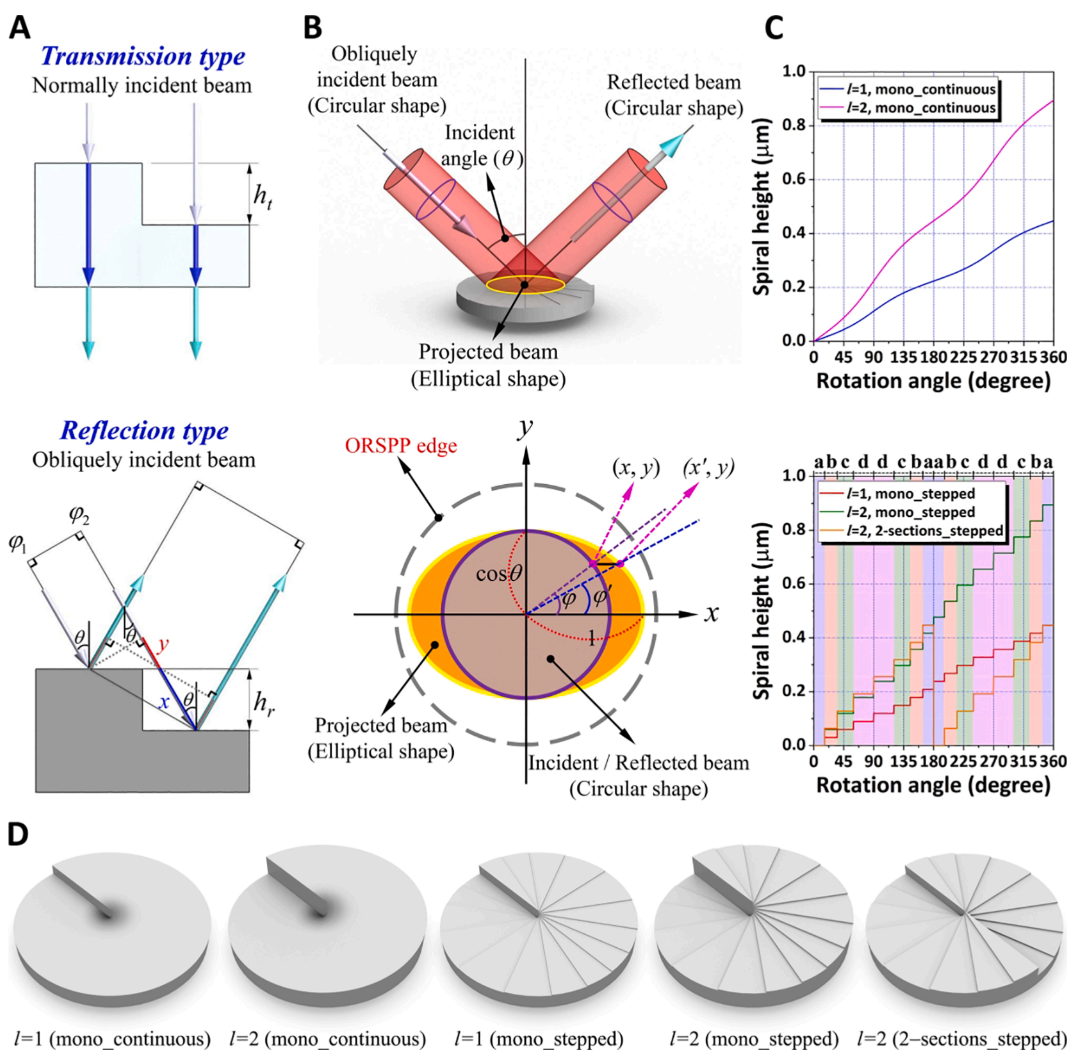


**Fig. 1.** A) Schematic diagrams for determination of $h_t$ (top) and $h_r$ (bottom) considering their differences in $\Delta L$. B) Geometry of the elliptical shape on ORSPP determined by obliquely incident beam. C) Variation of $H$ according to the rotation angle of CORSPPs (top) and SORSPPs (bottom). Lowercase alphabetical letters (a, b, c, and d) in the bottom figure represent a notation of a circular sector divided into 16-circular sectors and have the central angle of each circular sector ($\varphi$') such as 16.3, 18.9, 24.4, and 30.4°, respectively. D) Various types of designed ORSPPs for $l$ = 1 and 2, considering conditions such as $\lambda$ = 632.8 nm and $\theta$ = 45°.

$$H = \varphi'/(2\pi) \times h_r = \varphi'/(2\pi) \times \lambda/(2cos\theta)$$
$$= 1/(2\pi) \times \lambda/(2cos\theta) \times tan^{-1}[tan\varphi/sec\theta] \quad (2)$$

The variation of $H$ according to the rotation angle of continuous ORSPPs (CORSPPs) and stepped ORSPPs (SORSPPs) with $l$ = 1 and 2, which is given by Equation (2), has been plotted in Fig. 1C. To be more exact, $H$ variations for each ORSPP behave along the profile which curvature direction is varied per $m\pi/2$ (where $m$ is integer) due to the elliptical beam shape on ORSPP. For SORSPP, when using a He-Ne laser ($\lambda$ = 632.8 nm), each $h_{r\text{-}step}$ of 16-SORSPP for $l$ = 1 and 2, and that of the 2-sections SORSPP for $l$ = 2, becomes ~ 30 nm (=447/15), ~60 nm (=894/15), and ~ 64 nm (=447/7), respectively.

The central angles of circular sectors in SORSPP are different from one another because, as previously stated, the beam cross-section on ORSPP is elliptical. At the bottom of Fig. 1B, the blue dotted line that connects (0, 0) to ($x$', $y$) determines the central angle of each circular sector ($\varphi$') in a large circle. If the inner circle is divided into 16-circular sectors with equal angles of 22.5°, the large circle at the bottom of Fig. 1B is divided into 16-circular sectors with different central angles of each circular sector. As $\varphi' = \tan^{-1}[\tan\varphi/\sec\theta]$ (where $\varphi$ = 22.5°, 45°, 67.5°, and 90°, and $\theta$ = 45°), the angle ($\varphi$') of each circular sector in the first quadrant of the Cartesian coordinate system increases gradually, such as 16.3° (a) → 18.9° (b) → 24.4° (c) → 30.4° (d). Subsequently, the angle ($\varphi$') increases and decreases repeatedly during a single revolution (see the bottom of Fig. 1C).

On the basis of the geometry described above, we designed various types of ORSPPs for $l$ = 1 and 2 considering conditions such as $\lambda$ = 632.8 nm and $\theta$ = 45°, as shown in Fig. 1D. ORSPPs with $l$ = 1 have a structure in which $h_r$ corresponding to a phase difference of $2\pi$ (447 nm) within one revolution (360°) is attained by a continuous rise or a 16-stepped rise. In the case of ORSPPs with $l$ = 2, two different design approaches were adopted to produce $l$ = 2: one in which $h_r$ corresponding to a phase difference of $4\pi$ (894 nm) is reached monotonically within one revolution (360°), and another in which one section for which $h_r$ corresponding to a phase difference of $2\pi$ (447 nm) is divided into 8 steps is repeatedly placed two times in one revolution (360°). These designs can help obtain a clear insight into the difference in optical characteristics between ORSPPs having the same $l$ but dissimilar structure.

## Results and discussion

### *Verification via numerical simulation*

It is imperative to validate the design described above by confirming whether the designed ORSPPs generate beams with characteristics of LG vortex beams. To do so, we performed 3D electromagnetic (EM) wave simulations based on the finite element (FE) method. To mimic the laser beam reflection that occurred by ORSPP, each 3D FE model was constructed with fairly large dimensions of 13 μm × 13 μm × 12 μm (from the perspective of wave optics simulation) with over $10^8$ degrees of freedom, and was comprised of two calculation domains: the ORSPP and the surrounding air domain. To reduce the computational cost, the ORSPP domain was modeled as a diameter of 7.5 μm maintaining $h_r$ of each ORSPP structure, and the surrounding air domain was truncated by the scattering boundary condition, which makes a boundary transparent for all outgoing EM waves with mathematically small reflections. We considered that the uniform plane wave (linearly polarized (LP) and circularly polarized (CP) incident beams) with a wavelength of 632.8 nm was incident on a surface of the ORSPP at an angle of 45°. FE analyses were implemented by solving the full-field formulation in the frequency domain, defined as:

$$\nabla \times \mu_r^{-1}(\nabla \times \boldsymbol{E}) - \frac{\omega^2}{c_0^2}\left(\varepsilon_r - \frac{i\sigma_{elec}}{\omega\varepsilon_0}\right)\boldsymbol{E} = 0 \quad (3)$$

where $\mu_r$ is the relative permeability; **E** is the electric field; $\omega$ is angular frequency; $c_0$ is the speed of light in a vacuum; $\varepsilon_r$ is relative permittivity; $\sigma_{elec}$ is electrical conductivity; and $\varepsilon_0$ is the permittivity of a vacuum. Here, $\mu_r$ was assumed to be 1, and the frequency-dependent complex refractive index ($n$) was applied to each calculation domain instead of $\sqrt{(\varepsilon_r - \frac{i\sigma_{elec}}{\omega\varepsilon_0})}$ (the Johnson model [22] for Ni and the data of Ciddor [23] for air). Then, the distributions of the time-averaged Poynting vector, phase, and time-averaged AM densities of the laser beam propagating in free-space were numerically calculated by employing the obtained FE results. Here, the commercial FE software COMSOL Multiphysics (Version 5.5, COMSOL Inc., Palo Alto, CA) was employed to perform the

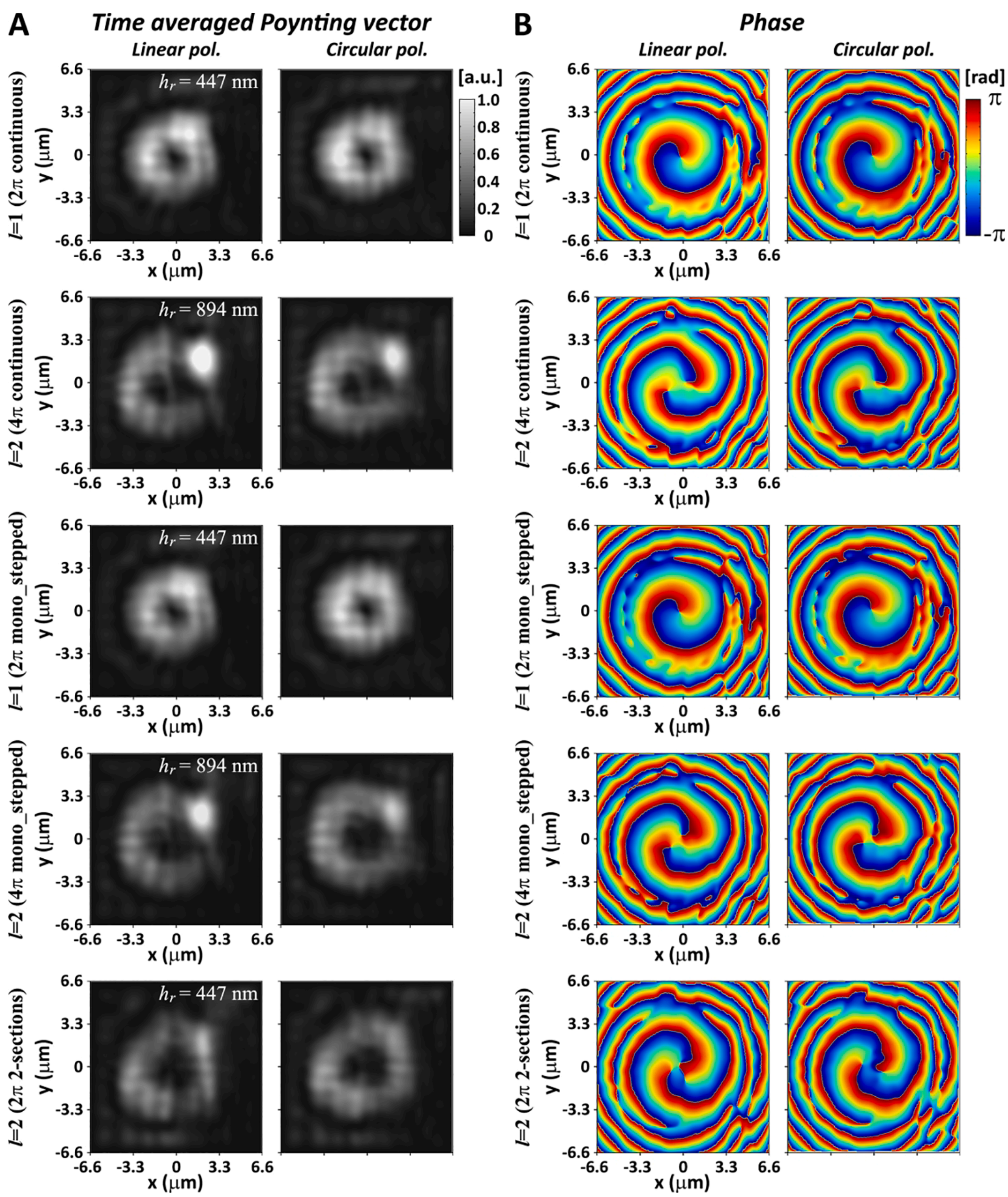


**Fig. 2.** Distributions in the transverse plane of A) the time-averaged Poynting vector normalized by the arbitrary value of the global time-averaged Poynting vector, and B) the phase plotted from $\pi$ to $-\pi$, for each laser beam reflected by the designed ORSPPs. Note that the positions of the transverse plane that acquired calculation values were fixed to the top surface of the 3D FE models constructed with the same dimension for each ORSPP; however, the propagation distance from the ORSPP center ($z_d$) was somewhat different according to each $h_r$; $z_d$ = 8.84 and 8.68 μm for $h_r$ = 447 and 894 nm, respectively.

FE analyses.

Fig. 2 depicts the distributions of the normalized time-averaged Poynting vector and the phase in the transverse ($x$-$y$) plane located at the far-field zone (exactly 8.84 μm for $h_r = 447$ nm and 8.68 μm for $h_r = 894$ nm away from ORSPP center), for all designed ORSPPs, under LP and CP incident beams. As can be seen from Fig. 2A, patterns of the time-averaged Poynting vector distributions formed into an exact annular shape in all designed ORSPPs regardless of $l$, geometric structure of ORSPP (having the same $l$ but different surface structures), and the state of polarization (SOP) of the incident beam. With increasing $l$, the outer diameter and dark central region of the beam expanded and the intensities distributed tended to decrease. Also, in the comparison between ORSPPs with the same $l$ but different structures, we found that there were no significant intensity differences despite the change in diffraction characteristics in accordance with the disparate geometric structures. Strangely, in the case of $h_r = 894$ nm, we found the local area, where the exorbitantly high values of the time-averaged Poynting vector were distributed, within an annular zone. However, it was assumed to be negligible as it may be induced by the excessive scattering that occurred from the drastic alteration of the spiral height at the end of the spiral surface. Also, this phenomenon may be due to the considerably close position of the transverse ($x$-$y$) plane, which can contain light that is irrelevant to the formation of LG vortex mode. Fig. 2B reveals the total phase change in the transverse plane perpendicular to the beam axis. Depending on $l$, continuous phase changes of $2\pi$ appeared cyclically with the spiral shape on one rotation around the optical axis. The total phase change for ORSPPs with $l = 1$ was obviously $2\pi$, and that for each ORSPP with $l = 2$ was undoubtedly $4\pi$. Similar to the time-averaged Poynting vector distributions, no significant differences in the phase distributions were found under different geometric structures or SOP of the incident beam. These EM simulation results for the time-averaged Poynting vector and the phase showed the characteristics of typical LG vortex modes, and they are well coincident with literature [13,24]. Consequently, at least numerically, the designed ORSPPs were able to reproduce the LG vortex beams.

We further analyzed the optical AM, which is one of the dynamic characteristics of EM waves and plays a vital role in light-matter interactions [25–27]. It is now well understood that optical AM generates an optical torque on particles, causing their dynamic rotation [10,28,29]. It consists of two components: spin angular momentum (SAM), which is possessed by right-handed or left-handed CP light, and OAM, which originates from the azimuthal phase gradient of the light [28,29]. Analogously, the physical quantity representing the time-averaged AM per unit volume (called the time-averaged AM density, $<\mathbf{j}>$) can be separated into the spin part $<\mathbf{j}_{spin}>$ and orbital part $<\mathbf{j}_{orbital}>$. For a monochromatic light field, these two components can be expressed as:

$$<\boldsymbol{j}_{spin}> = \frac{Im[\varepsilon_0 \boldsymbol{E}^* \times \boldsymbol{E}]}{2\omega} \tag{4}$$

$$<\boldsymbol{j}_{orbital}> = \boldsymbol{r} \times \frac{Im[\varepsilon_0 \boldsymbol{E}^* \cdot (\nabla) \boldsymbol{E}]}{2\omega} \tag{5}$$

where $\mathbf{r}$ is the position vector; and $\boldsymbol{E}^* \cdot (\nabla)\boldsymbol{E} = E_x^* \nabla E_x + E_y^* \nabla E_y + E_z^* \nabla E_z$ [26,30–34]. Using Eqs. (4) and (5), we separately calculated these two AM densities on the basis of the FE results obtained from the EM wave simulations described above. Note that because SAM does not physically exist under LP light (it means that $<\mathbf{j}>$ equals $<\mathbf{j}_{orbital}>$), we only plotted the calculated results on the CP incident beam.

Fig. 3 exhibits the distributions of the time-averaged SAM and OAM densities in the transverse ($x$-$y$) plane located in the same position as Fig. 2. Overall, patterns of the time-averaged SAM and OAM densities for each ORSPP were almost identical to each other, except that the magnitudes of the time-averaged OAM densities were approximately 1–1.5 orders of magnitude higher than those of the time-averaged SAM densities. These are in good agreement with the previous results [34,35]. Moreover, patterns of these AM densities were similar to those of the time-averaged Poynting vector (see Fig. 2A). As the AM densities are theoretically derived from the Poynting vector, which represents the rate of EM energy per unit area [35,36], the obtained patterns of these AM densities may be a naturally expected result. From the calculated results for the time-averaged AM densities, we confirmed the existence of these densities in the laser beam reflected by the designed ORSPPs.

The aforementioned numerical results depicted archetypal LG vortex beam characteristics: 1) annular intensity distributions with the singular point, where the phase is undefined (called the phase singularity), were indicated; 2) the size of the dark central area of the beam enlarged with

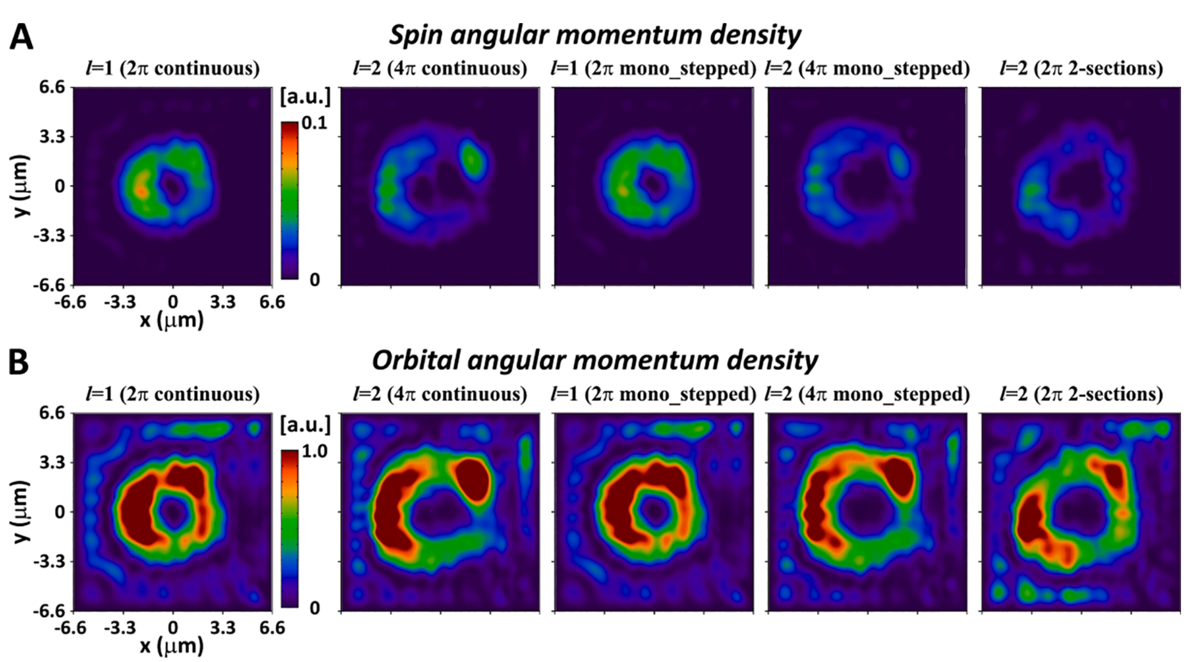


**Fig. 3.** Distributions in the transverse plane of A) the normalized SAM density, and B) the normalized OAM density, for each laser beam reflected by the designed ORSPPs, when applying the CP incident beam. Note that the values of the SAM density are normalized by the same value used in the OAM density.

an increase of $l$; 3) the phase rotated azimuthally around the phase singular point, characterized by the phase factor $e^{il\Phi}$, where $\Phi$ is the azimuthal angle; and 4) the SAM and OAM components existed in the laser beam propagating in free-space. Therefore, we confirmed that each beam reflected by the designed ORSPPs was clearly an LG vortex beam and we finally concluded that our geometric designs were suitable for fabricating large-sized ORSPPs.

*Hybrid-mechanical fabrication*

Unlike transmissive SPPs with micro-scale $h_t$ values, which are generally produced by a series of lithographic processes, the fabrication of large-sized (over 100 mm diameter) ORSPPs with sub-micro-scale $h_r$ values using metallic materials is particularly challenging using conventional technologies. In this study, the large-sized ORSPPs using nickel-phosphorus plated aluminum with a diameter of 100 mm were incarnated by utilizing the hybrid-mechanical processing technique. For SORSPPs, the combined machining system, composed of a three-axis ultraprecision DTM (Nanoform 1000, Precitech) and FTS (FTS-1000, Precitech), was used, as shown in Fig. 4A. This combined machining system, through only one machining process, enabled us to mechanically manufacture metallic materials with low surface roughness over a large area and to obtain a high form accuracy, especially the sharp edges, in segments of ORSPPs. The large-sized ORSPPs had an asymmetric geometry joined by fan-shaped segments having each $h_{r\text{-}step}$ of a few tens of nanometers around the axis of rotation. Therefore, the aforementioned technique for manufacturing the non-rotationally symmetric surface, in which the diamond tool of the machining system moved along the arc direction on cylindrical coordinates during machining (different from a typical machining process that adopts Cartesian coordinates [37,38]), was considered. This technique diminished the tool interference around the center of an ORSPP and was advantageous in making the sharp edges of the ORSPP segments. For CORSPPs, the MRF polishing process was supplementally taken into account in addition to the DTM-FTS processes that performed the role here to manufacture the base of the continuous surface (see Fig. 4B). The base of the continuous surface and the edge positioned at the end of the spiral surface were precisely formed within the performance limits of the DTM-FTS machining system. Afterward, the MRF polishing machine (Q-Flex 300, QED Technologies) was used successively to correct the surface figure errors that occurred during the DTM-FTS processes to the designed continuous surface (see the top of Fig. 1C).

All ORSPP designs (see Fig. 1D) were fabricated and then the 3D geometric structures (including $h_{r\text{-}step}$ for each fabricated ORSPP) were confirmed using Fizeau interferometer (S150, Apre). As shown in Fig. 5A, the spiral patterns of all fabricated ORSPPs were almost identical to the designed ones, although the diameter of all fabricated ORSPPs is quite large to be a diameter of 100 mm. In particular, it is not difficult to find that each $h_{r\text{-}step}$ of a few tens of nanometers in SORSPPs and smoothly and continuously increased spiral height in CORSPPs were certainly formed. From the obtained 3D surface topographies displayed in Fig. 5A, line profiles for the spiral height variation along with the rotation angle with respect to the center of each ORSPP were acquired (see Fig. 5B). In this figure, for CORSPPs with $l = 1$ and 2 (denoted by the solid lines with blue and magenta colors, respectively), the spiral heights within a single revolution increased up to ~450 nm and ~900 nm, respectively. These results were similar to the theoretical values formed by Equation (2) (see the top of Fig. 1C). For 16-SORSPPs with $l = 1$ and 2 (denoted by the red and olive solid lines, respectively), the spiral heights formed 16 steps along the continuous line profiles. The 2-sections SORSPP formed a spiral height of ~450 nm (in response to $2\pi$) at rotation angles of 180° and 360° (see the orange solid line). Overall, all SORSPPs showed that the width of each step repeatedly increased and decreased four times within one revolution, as mentioned above. And each $h_{r\text{-}step}$ for the 16-SORSPP with $l$ = 1 and 2, and the 2-sections SORSPP with $l$ = 2 was ~30, ~60, and ~65 nm, respectively.

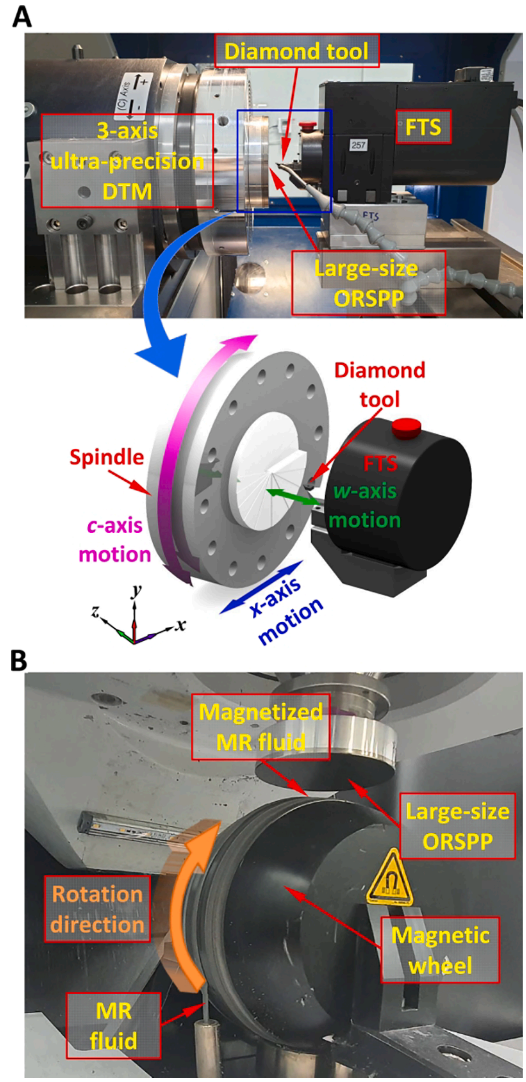


**Fig. 4.** A) Machining system that includes: three-axis ultraprecise DTM (Nanoform 1000, Precitech) and FTS (FTS-1000, Precitech). During machining, the maximum rotational speed of c-axis (the spindle rotational direction about the z-axis) is 500 rpm, and the maximum FTS stroke frequency of w-axis (the feed direction into the surface of the ORSPP and parallel to the z-axis) is 0.5 kHz with the maximum stroke length of 2 μm. B) MRF polishing is an optical fabrication method that uses the magnetorheological fluid and is well known as the deterministic process in the optical manufacturing field. During corrective polishing, a 20 mm dia. magnetic wheel rotates at 1857 rpm and the flow rate of the magnetorheological fluid sprayed at the wheel surface is 0.18 lpm. These machining conditions generate a removal function that is 0.6550 μm/min in peak removal rate and 0.0023 mm$^3$/min in volume removal rate. During both processes, a temperature control system was used to minimize form errors by restricting the temperature fluctuation within ±0.02 °C inside the machining systems.

However, for 16-SORSPP with $l = 1$, the manufacturing process becomes more difficult due to the half-height of $h_{r\text{-}step}$ compared to that with $l = 2$; hence, its edge slope that forms $h_{r\text{-}step}$ was a little gentle compared to 16-SORSPP with $l$ = 2 and the 2-sections SORSPP.

The improvement in surface roughness by the MRF polishing process in addition to the DTM-FTS processes was noticeable. The surface roughness was measured using a coherence correlation interferometer (CCI Optics, Taylor Hobson) for two ORSPPs: 1) 16-SORSPP with $l$ = 1 manufactured via the DTM-FTS processes, and 2) CORSPP with $l$ = 1 manufactured via sequential DTM-FTS processes + MRF polishing process. As shown in Fig. 5C, the 2D image of the surface roughness

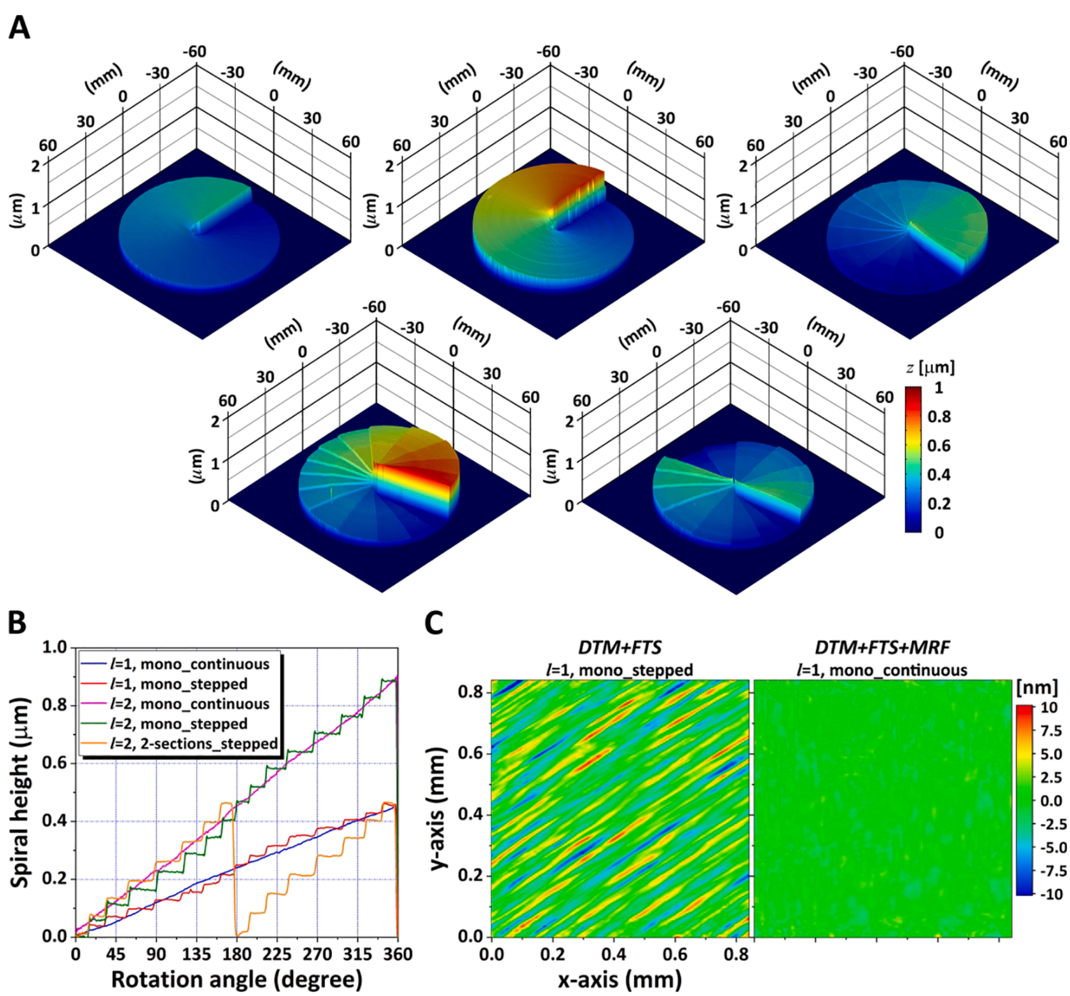


**Fig. 5.** A) 3D surface topographies of the fabricated ORSPPs observed using Fizeau interferometer. Note that because the spiral height of each ORSPP is relatively very small compared with a diameter of that, we plotted using different dimension scales as $x$, $y$ = mm and $z$ = μm. B) Line profiles on the variation of the spiral height according to an increase of the rotation angle from 0 to $2\pi$. Five cases are presented according to their ORSPPs in Fig. 5A. C) 2D surface roughness for two ORSPPs. The left figure denotes the result of SORSPP with $l$ = 1 manufactured via the DTM-FTS processes and the right figure shows that of CORSPP with $l$ = 1 manufactured via the DTM-FTS processes + MRF polishing process.

obtained via the DTM-FTS processes + MRF polishing process (right figure) was improved compared to that obtained via the DTM-FTS processes (left figure). In the left of Fig. 5C, the modulation by the toolmark of the DTM occurred with a height of ~ ±10 nm (this value is vastly superior to the results obtained from the typical DTM process) along the oblique direction. In the right of Fig. 5C, on the other hand, it can be seen that this modulation almost disappeared and the height distribution as a whole was within ~ ±2 nm, as can be seen from the color bar. Quantitatively, for these two cases, the Sa (arithmetic mean height) values, which are used generally to evaluate the area surface roughness, were 2.6 nm and 0.6 nm, respectively.

*Experimental demonstration*

Next, we experimentally demonstrated the optical performance of the fabricated large-sized ORSPPs through 2D far-field imaging (see Fig. 6). Fig. 7A shows far-field images of the intensity distributions observed under LP and CP incident beams. As we intended and expected, all reflected beams presented annular intensity distributions with a dark central region, regardless of SOP of the incident beam. In addition, one can see that the outer diameter and dark central region of the beam enlarged with increasing $l$. These experimental results approximately corresponded with the EM wave simulation results reporting the distributions of the time-averaged Poynting vector and AM densities (see Fig. 2A and 3). We additionally demonstrated that all beams reflected by ORSPPs were the vortex mode by identifying the number of branches of fork interference fringes, which were obtained from the superposition of the plane reference beam and the beam reflected by ORSPP. As expected, the fork interference patterns, which depend on the quantity of $l$ for the LG vortex beams, were clearly observed around the central interference fringes, as shown in Fig. 7B. As the number of extra fringes at each singular point equals the number of $2\pi$ azimuthal phase change, two and three fork branches observed in this figure correspond to the quantity of $l$ = 1 and 2 of the LG vortex beams, respectively, regardless of the SOP [10,39]. These results also coincided with the simulation results showing the total phase change, according to $l$, of all designed ORSPPs. Consequently, judging from the obtained surface topography (see Fig. 5) and far-field imaging (see Fig. 7) results, we conclude that large-sized ORSPPs with $l$ = 1 and 2 were successfully made based on the proposed geometric design and hybrid-mechanical processing technique.

As mentioned earlier, the highest intensity LG vortex laser pulse, which is essential for ultrashort intense LPI, originated from low-order uniformed LG vortex laser pulses with well-defined OAM. In particular, as the LG vortex beam is extremely sensitive to wavefront deformation [40], not only the beam shape but also the uniformity of beam distribution formed along with the circumference of an annular zone could directly affect the focusability (and accordingly, peak intensity) of the LG vortex beam. Therefore, we analyzed in detail the intensity

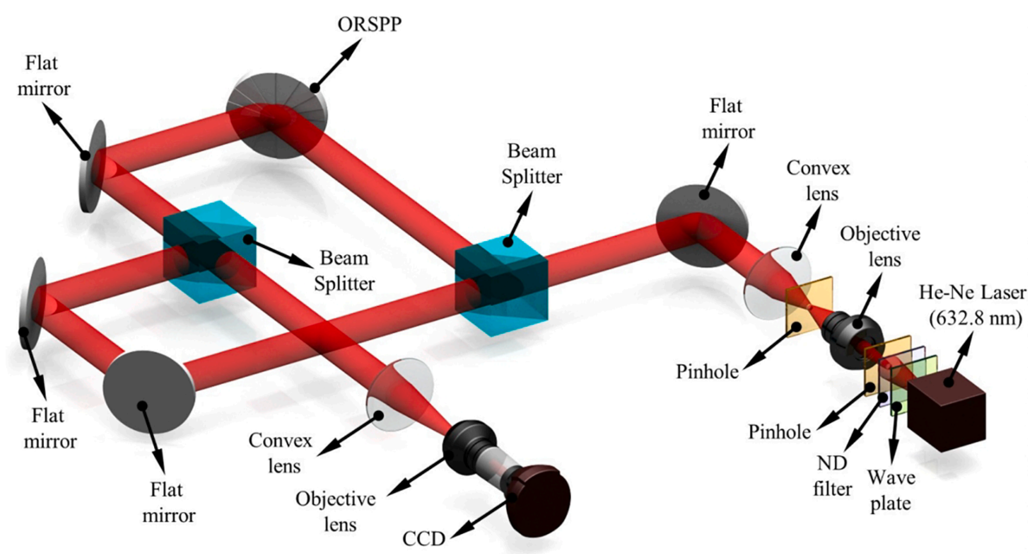


**Fig. 6.** Experimental configuration for measuring the images of the LG vortex beams and the interference fringes between the Gaussian and LG vortex beams using ORSPP. As a light source, an He–Ne laser ($\lambda$ = 632.8 nm) was used. A wave plate ($\lambda$/2 or $\lambda$/4) and neutral density (ND) filter were used to change the polarization and attenuate the beam energy, respectively. For the spatial filtering of the beam, an objective lens (f = 200 mm, 20×) and two pinholes were applied. In addition, through a convex lens (f = 150 mm), an enlarged collimated beam was obtained. After reflection on a flat mirror (gold-coated), the collimated beam was incident on a modified Michelson-typed interferometer, which consists of two beam splitters. Among them, one arm includes the ORSPP to form the LG vortex beams. And at second beam splitter, two beams (Gaussian and LG vortex beams) are combined. The beams are reduced via a convex lens (f = 500 mm), and it is imaged by a CCD behind the objective lens (f = 200 mm, 10×). For measuring the 2D images of the LG vortex beams, beam block is inserted in the arm that includes ORSPP.

uniformity of the LG vortex beams with $l = 1$ obtained from the experimental demonstration described above. Fig. 8 illustrates the intensity profiles along the *x*-axis, *y*-axis, and the circular lines for three radii (11.25, 15, and 18.75 μm) within an annular zone, plotted for CORSPP and 16-SORSPP. As shown in Fig. 8A, the intensity profiles along each axis (*x*- and *y*-axis) on both ORSPPs were similar to the shape of the LG mode beam profile with $l = 1$. However, there were some differences between two ORSPPs. For CORSPP, no significant differences between the two intensity peaks on the beam, which are represented by the height of the red box, were found in both axes profiles. However, for 16-SORSPP, these differences (represented by the height of the blue box) were considerably large in both axes profiles. This means that the intensity distributions within an annular zone were relatively uniform compared with 16-SORSPP. Fig. 8B shows the variations of the beam intensities along the circular lines within an annular zone. Three circumferences corresponding to the radii $r$ = 11.25, 15, and 18.75 μm denote the inner, middle, and outer position on an annular zone, respectively. On this account, it can be seen that the intensity distributions were going upward and downward on the whole with respect to zero. In all three circular lines, the intensity profiles of CORSPP produced relatively low fluctuations with respect to zero value, compared to that of 16-SORSPP. The standard deviations for the red solid line and the blue solid line for $r = 11.25$ μm were 2.98 and 6.76, respectively. For $r = 15$ μm, they were 2.55 and 5.60, respectively; whereas for $r = 18.75$ μm, they were 1.64 and 3.69, respectively. These results led to the fact that the intensity fluctuation within an annular zone of 16-SORSPP was more than 2.2 times compared to that of CORSPP. This difference in the uniformity of intensity distributions may be attributed to two factors. One is the geometric structure of ORSPP surface; the stepped structure having each $h_{r\text{-}step}$ of a few tens of nanometers unavoidably raises an involuntary scattering and this phenomenon may get exacerbated by increasing $h_{r\text{-}step}$, which is related to the number of spiral steps and $l$. The other factor is whether the MRF polishing process after the DTM-FTS processes adds or not; an unfavorable surface roughness according to the fabrication processes leads to random scattering that negatively influences the formation of a uniform beam distribution (see Fig. 5C). Eventually, both factors could be concluded in the irregular scattering caused by the surface structure and roughness of ORSPP.

*Exploration of high-quality low-order LG vortex laser pulses in ultrashort intense LPI*

In ultrashort intense LPI, the spatial beam modes of the laser pulse are a crucial parameter when trying to characterize the interactions [41,42]. Recently, much attention has been paid to the use of LG vortex laser pulses in ultrashort intense LPI. For momentum transfer from light to matter in ultrashort intense LPI, SAM and OAM could play important roles in terms of the total AM. To realize these ideas, it is crucial to have an SPP that can withstand intense laser pulses as existing transmissive SPPs can easily get damaged by ultrashort intense laser-induced nonlinear self-focusing, unlike ORSPPs, as previously stated. Therefore, ORSPPs described in this study can prove to be promising candidates for generating ultrashort intense laser pulses with AM.

In this regard, we now present a numerical study on AM transfer from light to matter in ultrashort intense laser-plasma interactions—one of the main applications of ORSPPs driven low-order ($l = 1$) LG vortex laser pulses. Specifically, we conducted 3D PIC simulations in which ultrashort intense laser pulses in LG vortex beam mode are focused onto a near-critical-density plasma foil. In this simulation, the laser pulse had a center wavelength of 800 nm, a $\sin^2$ temporal profile with a pulse duration of 20 fs (FWHM), a focal spot size of 3.0 μm (FWHM), and a pulse energy of 4.1 J. In Gaussian mode, the focal intensity was $10^{21}$ W/cm$^2$. The plasma foil as thick as the laser wavelength consisted of electrons and protons with a density of $2n_c$ for each species, where $n_c$ is the critical density for the wavelength of 800 nm. The whole simulation domain had a volume of 16 μm × 16 μm × 24 μm, which was divided into cells with a volume of 20 nm × 20 nm × 20 nm. Each cell had four computational particles for each species, and the absorbing boundary conditions were applied both to the field and to the particles. The time was set so as to make the pulse reach the foil at $t = 0$. The LG modes were specified with two integers, i.e., the OAM quantum number $l$ and SAM quantum number $s$ with respect to the laser propagation axis (the $z$-axis with $x = y = 0$). In the paraxial approximation, the ratio of the total AM to the total energy equals to $\hbar(l + s)/\hbar\omega$ [43]. This is reminiscent of the

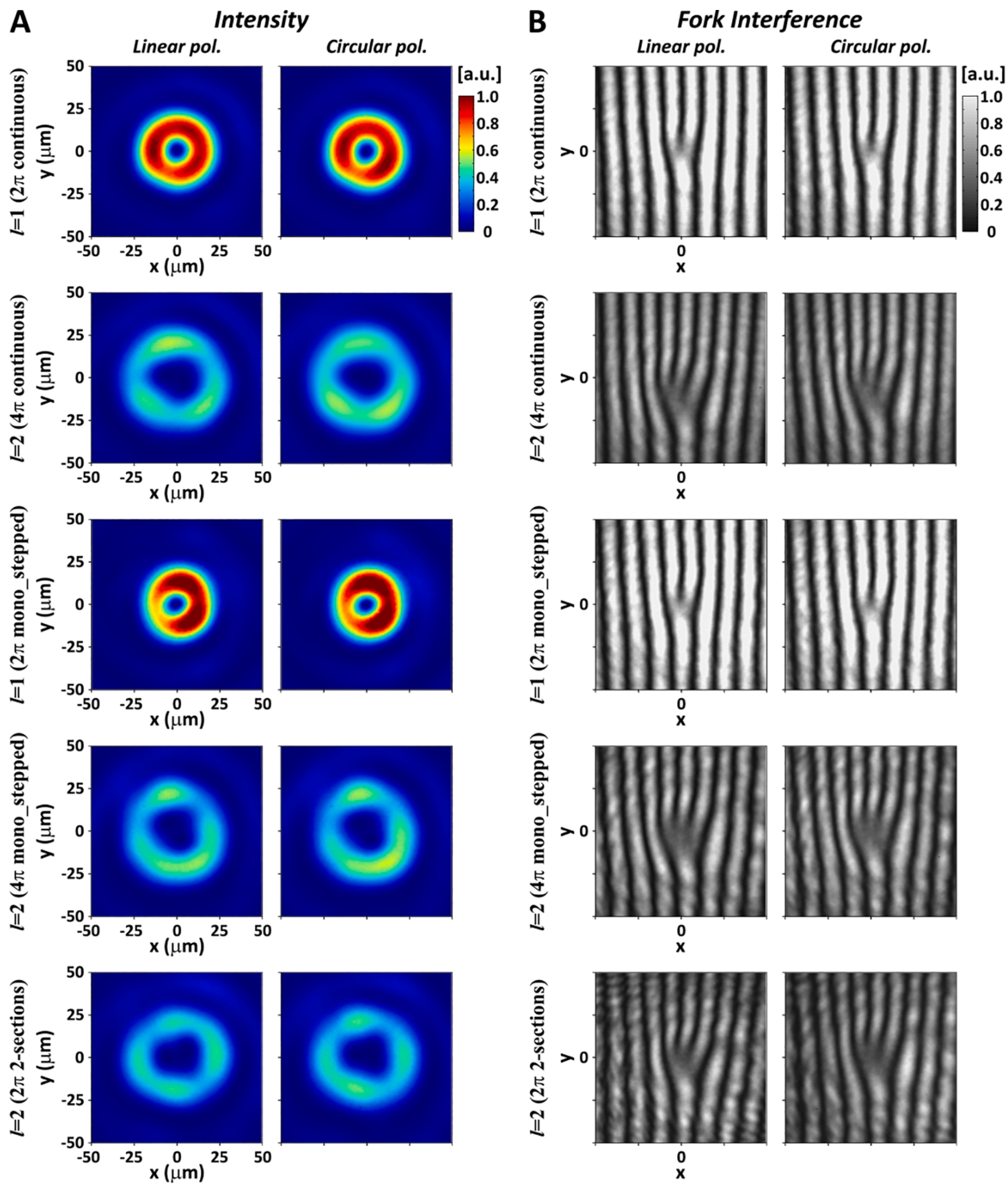


**Fig. 7.** A) 2D intensity distributions of LG vortex beam modes with OAM of topological charges $l = 1$ and 2 obtained under LP and CP incident laser beams by applying ORSPPs. B) Fork interference fringes obtained from the superposition of the plane reference beam and the LG vortex beam. Both distributions (Fig. 7A and 5B) were normalized by an arbitrary value of global intensity.

interpretation that each photon carries an AM of $\hbar(l+s)$ and an energy of $\hbar\omega$. For example, $(l = 0, s = 0)$ refers to the linearly polarized Gaussian mode, and $(0, \pm1)$ do to the circularly polarized Gaussian modes. The modes (0, 0), (1, 0), (0, −1), (1, −1), and (−1, −1) were considered in our simulation.

The left of Fig. 9A shows the electrons on a plane containing the laser propagation axis (the horizontal line with $y = 0$) after a pulse in the mode (1, −1) passes through the foil. Around and along the beam axis, the electrons gather forming dense regions, but, far from the axis, they spread outward (the regions unaffected by the pulse are neglected in the discussion). This behavior is attributed to the ponderomotive force near the focus. As the LG vortex mode with $|l| = 1$ has a hollow intensity profile at the focal plane [44], the mode provides an inward ponderomotive force near the beam axis and an outward force far from the axis. The right of Fig. 9A shows the protons in the same condition, which are displaced much less than the electrons because of their much larger mass (proton-to-electron mass ratio ~1836). Although the ponderomotive force on the protons is weaker than that on the electrons by the mass ratio, the Coulomb field due to the difference in displacement drives the protons so that the foil is shaped to conform the hollow intensity profile; the density is higher near the beam axis; and the foil near $y = \pm2$ μm is bent in the pulse's propagation direction.

The evolution of the plasma's AM around the beam axis is shown in Fig. 9B. Despite a much smaller displacement than electrons, the protons were found to have a larger AM. As the total AM is conserved for the combined system of the laser pulse and the plasma, we can interpret the sign changes in the plot as exchanges of AM between the laser pulse and the plasma. For the modes (1, −1) and (1, 0), the material AM changed its sign almost twice per optical period, and the maximum values were larger than those in the cases of other modes. Compared with the modes (1, −1) and (1, 0), the modes (0, −1) and (−1, −1) induced less frequent sign changes and lower maximum values. The interaction ceased at T = 16 cycles (~40 fs), after which the material AMs were virtually constant: $L_{1,-1} = -0.63$, $L_{0,-1} = -1.9$, $L_{-1,-1} = -4.2$, $L_{0,0} = -0.018$, and $L_{1,0} =$

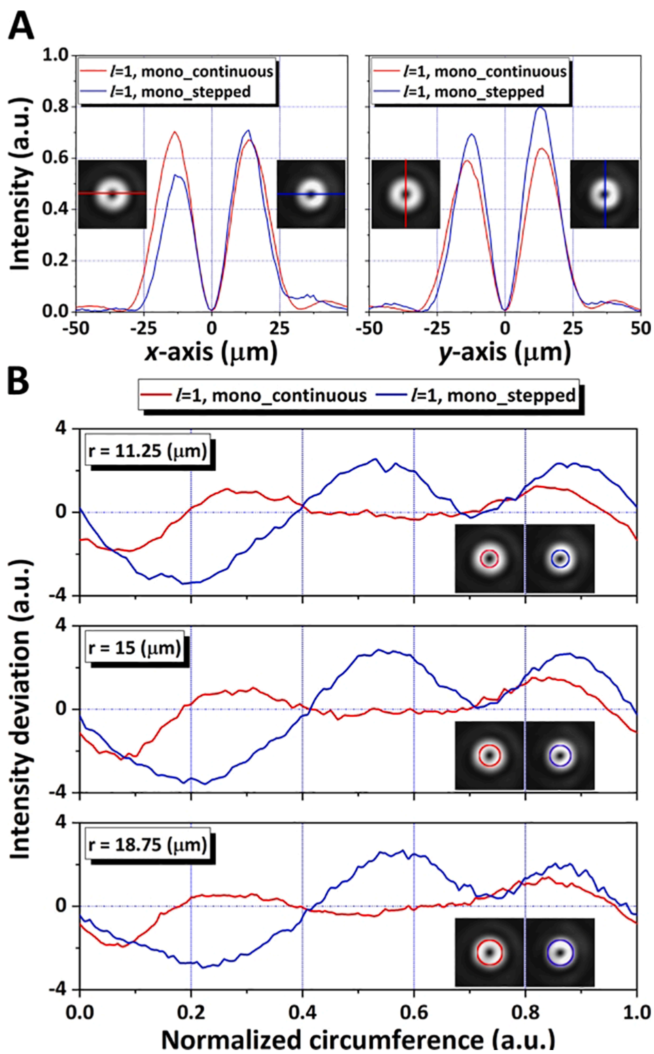


**Fig. 8.** Variations of the intensity profiles along A) the $x$-axis and $y$-axis, and B) along the three circular lines varied by three radii (r = 11.25, 15, and 18.75 μm) within an annular zone. In Fig. 8B, the $x$-axis indicates the normalized circumference and the $y$-axis represents the deviation value that subtracts its average value from the actual beam intensity distribution.

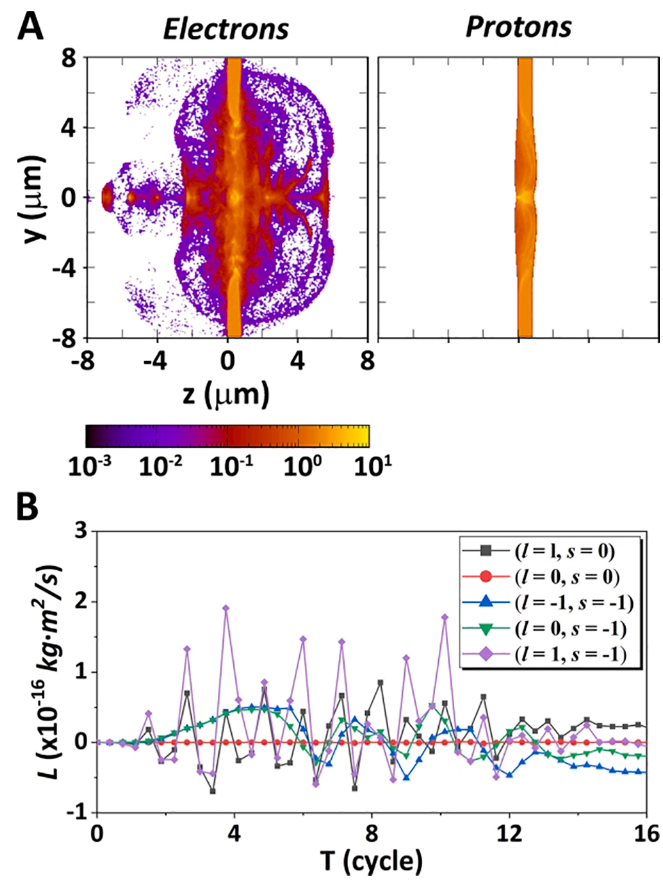


**Fig. 9.** Interaction of an ultrashort intense laser pulse with a near-critical-density plasma foil. The left figure of A) electron and right figure of 9A) proton distributions on the $y$-$z$ plane with $x = 0$ after passing of a pulse in the LG mode (1, −1) ($t$ = 30 fs). B) The variation in material angular momentum for the LG modes (1, −1), (0, −1), (−1, −1), (0, 0), and (1, 0).

2.2, where $L_{l,s}$ refers to the material AM induced by the mode ($l$, $s$) in units of $10^{-17}$ kg·m$^2$/s. These values are ordered roughly according to the value of total AM ($j = l + s$), indicating that the sum of the material AM and the total AM of laser is approximately conserved regardless of the specific field configuration. In Fig. 9B, we find interesting features. Both modes (1, −1) and (0, 0) have a null total AM ($j = 0$), but mode (1, −1) vigorously exchanges AM with the plasma in the course of interaction, whereas the mode (0, 0) has negligible exchange throughout. Similarly, both modes (0, −1) and (1, 0) have the same magnitude of total AM ($|j| = 1$), but mode (1, 0) is more vigorous in exchange. These observations imply that OAM and SAM are transferred in different manners, a clear understanding of which requires further investigation.

## Conclusions

In this study, based on our own geometric designs of ORSPP, we successfully obtained high-quality low-order ($l$ = 1 and 2) LG vortex beams with well-defined OAM generated from large-sized ORSPPs fabricated by applying the hybrid-mechanical processing technique. Through performing 3D EM wave simulations, the ORSPP designs were validated by calculating the Poynting vector, spiral phase changes, and AM densities. Characteristics of LG vortex beams that obtained from hybrid-machined ORSPPs were experimentally verified by observing of 2D intensity distributions and interference fringes. In particular, we analyzed the uniformity of annular beam shape in detail. The analyzed results showed that the intensity profiles of the LG vortex beams obtained from CORSPP produced relatively low fluctuations compared to that obtained from SORSPP, which may be due to the geometric structure of ORSPP and its surface roughness. As one of the main applications of ORSPPs driven low-order LG vortex laser pulses, in near future, it is expected that these results could prove to be essential in enabling researches to investigate high-intensity AM transfer from light to matter for various low-order LG vortex laser pulse modes—one of the fundamental interests in LPI. We believe that the high-quality low-order LG vortex beams generated using the large-sized ORSPPs introduced here have the potential to become one of the essential optical elements for research studies trying to discover novel phenomena in ultrashort intense LPI.

## Funding

Korea Basic Science Institute (D010300). Creative Convergence Research Project in the National Research Council of Science and Technology of Korea (CAP-15-01-KBSI). Institute for Basic Science (IBS) under IBS-R012-D1. Gwangju Institute of Science and Technology (GIST) under GIST Research Institute (GRI) grant in 2019.

## CRediT authorship contribution statement

**Ji Yong Bae:** Conceptualization, Methodology, Validation, Formal analysis, Investigation, Writing - original draft, Writing - review & editing, Visualization. **Cheonha Jeon:** Validation, Investigation. **Ki Hong Pae:** Formal analysis, Investigation. **Chul Min Kim:** Formal analysis, Investigation. **Hong Seung Kim:** Validation, Formal analysis. **Ilkyu Han:** Formal analysis. **Woo-Jong Yeo:** Resources. **Byeongjoon Jeong:** Resources, Visualization. **Minwoo Jeon:** Resources. **Dong-Ho Lee:** Visualization. **Dong Uk Kim:** Methodology. **Sangwon Hyun:** Methodology. **Hwan Hur:** Methodology. **Kye-Sung Lee:** Methodology, Funding acquisition. **Geon Hee Kim:** Methodology, Funding acquisition. **Ki Soo Chang:** Methodology, Funding acquisition. **Il Woo Choi:** Formal analysis. **Chang Hee Nam:** Methodology, Funding acquisition. **I Jong Kim:** Conceptualization, Methodology, Validation, Formal analysis, Investigation, Writing - original draft, Writing - review & editing, Supervision.

## Declaration of Competing Interest

The authors declare that they have no known competing financial interests or personal relationships that could have appeared to influence the work reported in this paper.

## References


[1] Mourou GA, Tajima T, Bulanov SV. Optics in the relativistic regime. Rev Mod Phys 2006;78:309.
[2] Vieira J, Mendonça JT. Nonlinear laser driven wakefields for positron and electron acceleration. Phys Rev Lett 2014;112:215001.
[3] Denoeud A, Chopineau L, Leblanc A, Quéré F. Interaction of ultraintense laser vortices with plasma mirrors. Phys Rev Lett 2017;118:033902.
[4] Brabetz C, Busold S, Cowan T, Deppert O, Jahn D, Kester O, et al. Laser-driven ion acceleration with hollow laser beams. Phys Plasma 2015;22:013105.
[5] Pae KH, Song H, Ryu C-M, Hee Nam C, Kim CM. Low-divergence relativistic proton jet from a thin solid target driven by an ultra-intense circularly polarized Laguerre-Gaussian laser pulse. Plasma Phys Control Fusion 2020;62:055009.
[6] Leblanc A, Denoeud A, Chopineau L, Mennerat G, Martin Ph, Quéré F. Plasma holograms for ultrahigh-intensity optics. Nat Phys 2017;13:440.
[7] Baumann C, Pukhov A. Electron dynamics in twisted light modes of relativistic intensity. Phys Plasma 2018;25:083114.
[8] Qiu CW, Yang Y. Vortex generation reaches a new plateau. Science 2017;357:645.
[9] Saleh BEA, Teich MC. Fundamentals of Photonics. Hoboken, NJ, USA: Wiley-Interscience; 2007.
[10] Yao AM, Padgett MJ. Orbital angular momentum: origins, behavior and applications. Adv Opt Photonics 2011;3:161–204.
[11] Wang X, Nie Z, Liang Y, Wang J, Li T, Jia B. Recent advances on optical vortex generation. Nanophotonics 2018;7:1533–56.
[12] Jiang Q, Bao Y, Li J, Tian L, Cui T, Sun L, et al. Bi-channel near-and far-field optical vortex generator based on a single plasmonic metasurface. Photonics Res 2020;8(6):986–94.
[13] Sueda K, Miyaji G, Miyanaga N, Nakatsuka M. Laguerre-Gaussian beam generated with a multilevel spiral phase plate for high intensity laser pulses. Opt Express 2004;12:3548.
[14] Massari M, Ruffato G, Gintoli M, Ricci F, Romanato F. Fabrication and characterization of high-quality spiral phase plate for optical applications. Appl Opt 2015;54:4077–83.
[15] Qian J, Peng Y, Li Y, Wang P, Shao B, Liu Z, et al. Femtosecond mid-IR optical vortex laser based on optical parametric chirped pulse amplification. Photonics Res 2020;8(3):421–5.
[16] Campbell G, Hage B, Buchler B, Lam PK. Generation of high-order optical vortices using directly machined spiral phase mirrors. Appl Opt 2012;51:873.
[17] Kim H, Bae JY, Jeong BJ, Kim GH, Chang KS, Kim IJ. Analysis of reflection type spiral phase plate for vortex beam generation. In: Proceedings of Nanophotonics and Micro/Nano Optics International Conference; 2019. p. 99.
[18] Shi L, Zhang Z, Cao A, Luo X, Deng Q. One exposure processing to fabricate spiral phase plate with continuous surface. Opt Express 2015;23:8620.
[19] Kotlyar VV, Almazov AA, Khonina SN, Soifer VA. Generation of phase singularity through diffracting a plane or gaussian beam by a spiral phase plate. J Opt Soc Am A 2005;22:849.
[20] Born M, Wolf E, Principles of Optics, seventh ed., Cambridge Univ. Press; 1999.
[21] Attwood D. Soft X-rays and Extreme Ultraviolet Radiation. Cambridge Univ. Press; 2007.
[22] Johnson PB, Christy RW. Optical constants of transition metals: Ti, v, cr, mn, fe, co, ni, and pd. Phys Rev B 1974;9:5056.
[23] Ciddor PE. Refractive index of air: new equations for the visible and near infrared. Appl Opt 1996;35:1566–73.
[24] Huo P, Zhang C, Zhu W, Liu M, Zhang S, Zhang S, et al. Photonic spin-multiplexing metasurface for switchable spiral phase contrast imaging. Nano Lett 2020;20(4):2791–8.
[25] Zhao Y, Edgar JS, Jeffries GD, McGloin D, Chiu DT. Spin-to-orbital angular momentum conversion in a strongly focused optical beam. Phys Rev Lett 2007;99(7):073901.
[26] Aiello A, Banzer P, Neugebauer M, Leuchs G. From transverse angular momentum to photonic wheels. Nat Photonics 2015;9(12):789–95.
[27] Bliokh KY, Nori F. Transverse and longitudinal angular momenta of light. Phys Rep 2015;592:1–38.
[28] Padgett M, Bowman R. Tweezers with a twist. Nat Photonics 2011;5(6):343–8.
[29] O'Neil AT, MacVicar I, Allen L, Padgett MJ. Intrinsic and extrinsic nature of the orbital angular momentum of a light beam. Phys Rev Lett 2002;88(5):053601.
[30] Bliokh KY, Bekshaev AY, Nori F. Extraordinary momentum and spin in evanescent waves. Nat Commun 2014;5:1–8.
[31] Berry MV. Optical currents. J Opt A: Pure Appl Opt 2009;11:094001.
[32] Cameron RP, Barnett SM. Electric–magnetic symmetry and Noether's theorem. New J Phys 2012;14:123019.
[33] Bliokh KY, Bekshaev AY, Nori F. Dual electromagnetism: helicity, spin, momentum and angular momentum. New J Phys 2013;15:033026.
[34] Zhang Y, Xue Y, Zhu Z, Rui G, Cui Y, Gu B. Theoretical investigation on asymmetrical spinning and orbiting motions of particles in a tightly focused power-exponent azimuthal-variant vector field. Opt Express 2018;26(4):4318–29.
[35] Bekshaev AY, Mikhaylovskaya LV. Electromagnetic dynamical characteristics of a surface plasmon-polariton. Optik 2019;186:405–17.
[36] Deng D, Guo Q. Airy complex variable function Gaussian beams. New J Phys 2009;11(10):103029.
[37] Li D, Qiao Z, Walton K, Liu Y, Xue J, Wang B, et al. Theoretical and experimental investigation of surface topography generation in slow tool servo ultra-precision machining of freeform surfaces. Materials 2018;11(12):2566.
[38] Gong H, Ao S, Huang K, Wang Y, Yan C. Tool path generation of ultra-precision diamond turning: a state-of-the-art review. Nanotechnol Precis Eng 2019;2(3):118–24.
[39] Franke-Arnold S, Allen L, Padgett M. Advances in optical angular Momentum. Laser Photon Rev 2008;2(4):299–313.
[40] Ohland JB, Eisenbarth U, Roth M, Bagnoud V. A study on the effects and visibility of low-order aberrations on laser beams with orbital angular momentum. Appl Phys B 2019;125:202.
[41] Shi Y, Shen B, Zhang L, Zhang X, Wang W, Xu Z. Light fan driven by a relativistic laser pulses. Phys Rev Lett 2014;112:235001.
[42] Wang W, Shen B, Zhang X, Zhang L, Shi Y, Xu Z. Hollow screw-like drill in plasma using an intense Laguerre-Gaussian laser. Sci Rep 2015;5:8274.
[43] Allen L, Padgett M. The Orbital Angular Momentum of Light: An Introduction. In: Torres JP, Torner L, (Eds.) Twisted Photons: Applications of Light with Orbital Angular Momentum, John Wiley & Sons; 2011, p. 1–12.
[44] Padgett M, Courtial J, Allen L. Light's orbital angular momentum. Phys Today 2004;57:35–40.